

See discussions, stats, and author profiles for this publication at: <https://www.researchgate.net/publication/3140428>

A Set of Image Processing Algorithms for Computer-Aided Diagnosis in Nuclear Medicine Whole Body Bone Scan Images

Article in IEEE Transactions on Nuclear Science · July 2007

DOI: 10.1109/TNS.2007.897830 · Source: IEEE Xplore

CITATIONS

23

READS

2,174

3 authors:



Jia-Yann Huang

Chang Gung Memorial Hospital

13 PUBLICATIONS 64 CITATIONS

SEE PROFILE



Pan-Fu Kao

Chung Shan Medical University

113 PUBLICATIONS 1,434 CITATIONS

SEE PROFILE



Yung-Sheng Chen

Yuan Ze University

280 PUBLICATIONS 2,428 CITATIONS

SEE PROFILE

The following manuscript was published in

Jia-Yann Huang, Pan-Fu Kao and Yung-Sheng Chen, **A set of image processing algorithms for computer-aided diagnosis in nuclear medicine whole body bone scan images**, *IEEE Transactions on Nuclear Science*, Vol. 54, No. 3, 514-522, 2007.

A Set of Image Processing Algorithms for Computer-Aided Diagnosis in Nuclear Medicine Whole Body Bone Scan Images

Jia-Yann Huang¹, Pan-Fu Kao², and Yung-Sheng Chen^{1*}

¹ Department of Electrical Engineering, Yuan Ze University, Chungli, Taiwan, R.O.C.

² Department of Nuclear Medicine, Buddhist Tzu Chi General Hospital, Hualien, Taiwan,
R.O.C.

** Correspondence author:*

- e-mail: eeyschen@saturn.yzu.edu.tw
- Tel: +886-3-4638800 ext 2409
- Fax: +886-3-4639355
- Address: 135 Yuan-Tung Road, Chungli, Taiwan 320, ROC

Running title: **Automatic CAD for Whole Body Bone Scan**

ABSTRACT

Adjustment of brightness and contrast in nuclear medicine whole body bone scan images may confuse nuclear medicine physicians when identifying small bone lesions as well as making the identification of subtle bone lesion changes in sequential studies difficult. In this study, we developed a computer-aided diagnosis system, based on the fuzzy sets histogram thresholding method and anatomical knowledge-based image segmentation method that was able to analyze and quantify raw image data and identify the possible location of a lesion. To locate anatomical reference points, the fuzzy sets histogram thresholding method was adopted as a first processing stage to suppress the soft tissue in the bone images. Anatomical knowledge-based image segmentation method was then applied to segment the skeletal frame into different regions of homogeneous bones. For the different segmented bone regions, the lesion thresholds were set at different cut-offs. To obtain lesion thresholds in different segmented regions, the ranges and standard deviations of the image's gray-level distribution were obtained from 100 normal patient whole body bone images and then, another 62 patient images were used for testing. The two groups of images were independent. The sensitivity and the mean number of false lesions detected were used as performance indices to evaluate the proposed system. The overall sensitivity of the system is 92.1% (222 of 241) and 7.58 false detections per patient scan image. With a high sensitivity and an acceptable false lesions detection rate, this computer-aided automatic lesion detection system is demonstrated as useful and will probably in the future be able to help nuclear medicine physicians to identify possible bone lesions.

Keywords: Computer-aided diagnosis (CAD); Whole body bone scan; Fuzzy sets; Image segmentation; Automatic lesion detection

1. INTRODUCTION

The main applications of nuclear medicine whole body bone scans include the detection of malignancy with bone metastasis together with bone infection such as osteomyelitis (Brown, 1989; Robey and Schellhanner, 1984). The whole body bone image is acquired in anterior view (\mathbf{I}_{AP}^{org}) and posterior view (\mathbf{I}_{PA}^{org}) by a scintillation gamma camera as shown in Fig. 1. Nuclear medicine technologists may adjust the brightness and contrast of whole body bone images before presenting the images as a film or on a display system. Nuclear medicine physicians make a diagnosis by inspecting these images and searching for abnormal lesion activity. Such a procedure has one major drawback, which is that different technologists may set different parameters for the image display system, This has the result that a non-standardized imaging display format may confuse physicians when identifying small bone lesions or determining subtle bone lesion changes in sequential studies.

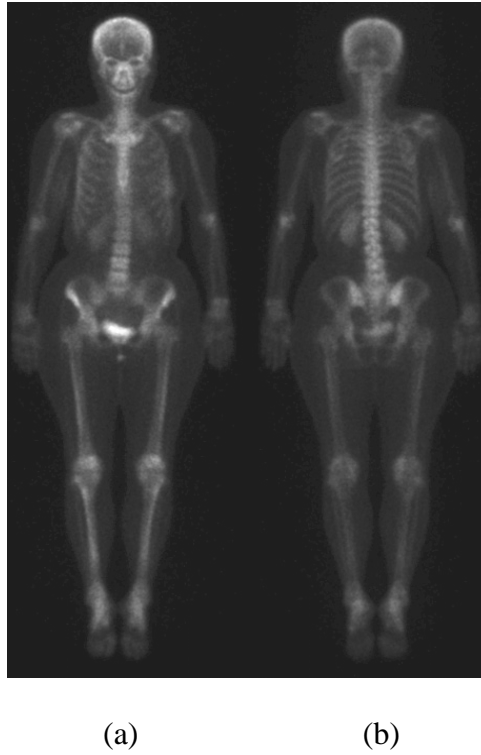


Fig. 1. Illustrations of a nuclear medicine whole body bone scan images in (a) anterior view and (b) posterior view, denoted as \mathbf{I}_{AP}^{org} and \mathbf{I}_{PA}^{org} respectively.

Computer-aided diagnosis (CAD) system applications for nuclear medicine whole body bone scans are quite limited in number. Erdi et al. (1997) reported a CAD system using the region growing method to estimate the survival time of a prostate cancer patient. That system was a semi-automatic method in which physician put a seed into a specific bone lesion and then computer grew the lesion area. In a recent study, Yin and Chiu (2004) employed a characteristic-point-based fuzzy inference system (CPFIS) to locate bone lesions. Radioactivity asymmetry and brightness were chosen as the two information inputs for the CPFIS, which were considered according to physicians' expertise and training. In that study, the whole body bone images were segmented into six parts, head, chest, vertebra, hand, pelvic, and leg, manually. Each part applied a different CPFIS. This system had a sensitivity of 91.5% (227 of 248) and the mean number of false positives (FPs) was 37.3 lesions per image. The high false positive rate resulted in the nuclear medicine physicians have to spend a lot of time discarding these false positive lesions. Šajn et al (2005) proposed a robust knowledge-based methodology for detecting reference points within the main skeletal regions, and the reference points were used for automatic segmentation of the skeleton. Interestingly, then the ArTeX and SVM algorithms were applied for diagnosis. To our knowledge, this system was the first completely automatic method for whole body bone scan diagnosis. After experimenting, the sensitivity was 79.6% and the specificity was 85.4%. The low sensitivity of this system resulted in the nuclear medicine physicians having to spend significant time looking for undetected lesions. Sadik et al (2006) adopted a set of segmentation algorithms and then used an artificial neural networks to detect bone lesions. Fourteen features were used as the input to the artificial neural networks. With this system, the sensitivity was 90% and the specificity was 74%; thus, because the specificity was low, it had the same drawbacks as the study of Yin and Chiu.

Due to the limitations of the above mentioned studies, we wished to develop a fully automatic lesion detection system that had high sensitivity and having acceptable false positive rate for use in clinical diagnosis. In this way, we developed a CAD system based on fuzzy sets histogram thresholding method and an anatomical knowledge-based image segmentation method that was able to analyze and quantify raw image data and identify the possible location of lesions. Using a more sophisticated segmentation method for the whole body bone scan images and applying different cut-offs in the different regions of homogeneous bone together with fully automatic lesion detection, we expected such a CAD program might be a practical help to nuclear medicine physicians and provide accurate in identification of the potential locations of bone lesions.

2. PROPOSED ALGORITHMS

The algorithms of the CAD system consist of three main steps: pre-processing, image segmentation, and lesion gray level determination. The first step includes (a) removing the noise outside the body region; (b) the application of Gaussian smoothing filter to compress the influence of noise inside the body region; (c) the adoption of a histogram equalization method to enhance image quality; and (d) deciding the true body frame size in the whole body bone image. The second step is to segment the whole body bone image into 46 homogeneous regions and to remove unexpected areas such as urine activity in bilateral kidney and bladder areas. Finally, the third step is devoted to determining the lesion gray level in each segmented homogeneous region and to determine the location of any lesion.

2.1. Pre-processing

The noise outside the body region were clearly visible on an over adjusted brightness image (Fig. 2a). The histogram of the image revealed a deep valley between two peaks at the low gray level area (Fig. 2d). A threshold value at valley of the histogram was applied to eliminate noise outside the body region.

The noises inside the body region were smoothed by adopting a Gaussian smoothing filter to the histogram. The form was isotropic, zero-mean Gaussian, expressed by:

$$G(x, y) = \frac{1}{2\pi\sigma^2} e^{-(x^2+y^2)/2\sigma^2} \quad (1)$$

To smooth the noisy whole body bone image, we applied an approximation involving a 5 by 5 convolution mask with a standard derivation (σ) of 1.4 as below:

$$\frac{1}{115} \begin{bmatrix} 2 & 4 & 5 & 4 & 2 \\ 4 & 9 & 12 & 9 & 4 \\ 5 & 12 & 15 & 12 & 5 \\ 4 & 9 & 12 & 9 & 4 \\ 2 & 4 & 5 & 4 & 2 \end{bmatrix}$$

For histogram equalization, a monotonic non-linear mapping was applied to reassign the gray-level values of pixels in the input image. After processing, the output image contains a uniform intensity distribution. The transfer function f is defined as:

$$f(\mathbf{I}_A) = g_{\max} \int_1^{h_{\max}} p_A(u) du \quad (2)$$

Where \mathbf{I}_A is the input image that was obtained after the noises removing procedure, g_{\max} is the maximum gray-level value (255 in an 8-bit gray-level scale), h_{\max} is the maximum gray-level value for \mathbf{I}_A , and $p_A(u)$ is the probability mass function of \mathbf{I}_A . The true body frame area of the equalized image can be obtained by detecting the rightmost, leftmost, topmost, and bottommost extremities of the body frame, and was denoted as \mathbf{I}_{AP}^{pre} (Fig. 2b) in anterior view. Fig. 2e shows the histogram of the equalized whole body image in anterior

view. The equalized image is helpful when further processing the fuzzy histogram threshold in order to prevent over thresholding.

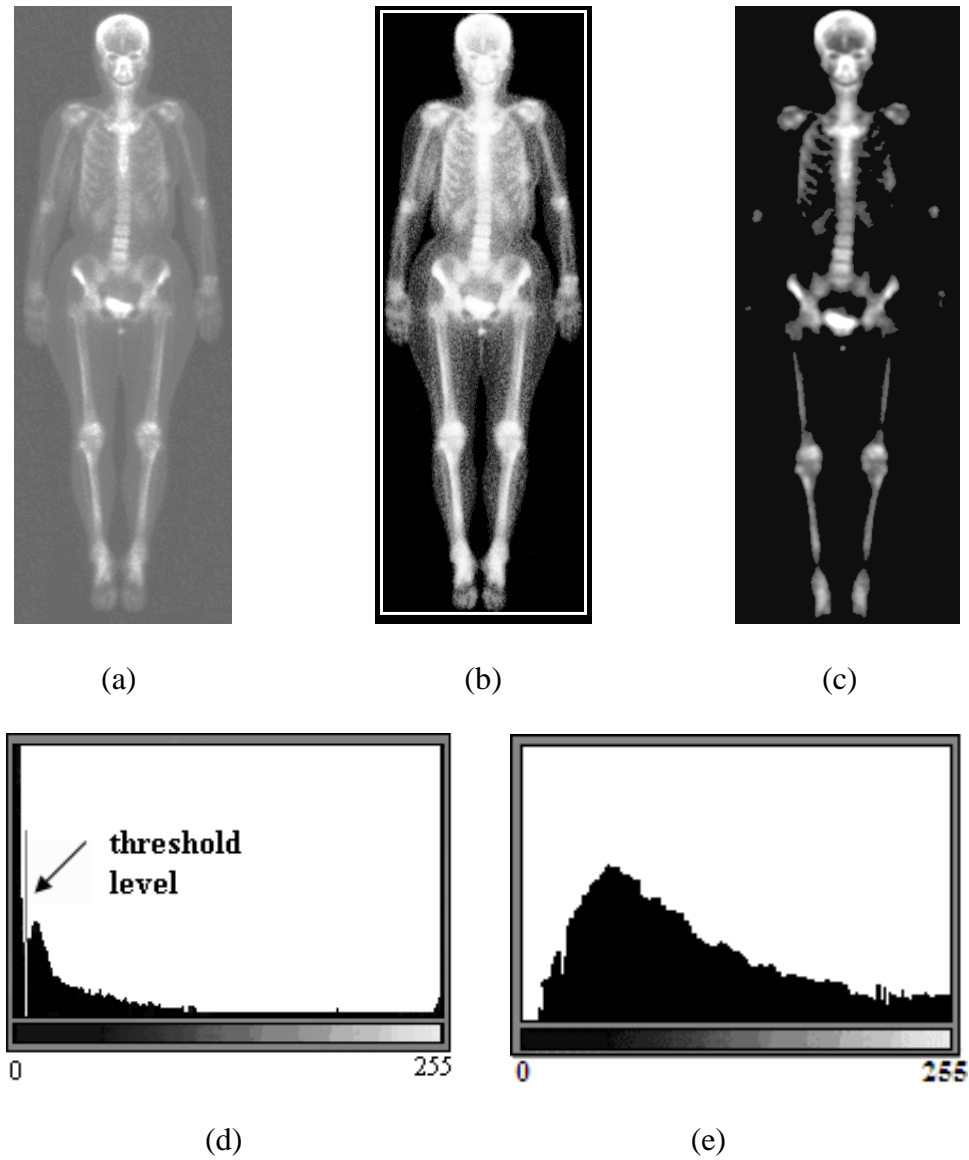


Fig. 2. A whole body bone image with noises distribution outside the body frame in (a) anterior view (I_{AP}^{org}) and its (d) histogram. After the pre-processing procedure, the whole body bone image is displayed in (b) anterior view (I_{AP}^{pre}) with its (e) histogram. The result of the fuzzy sets thresholding are shown in (c) the anterior view (I_{AP}^{fuzzy}).

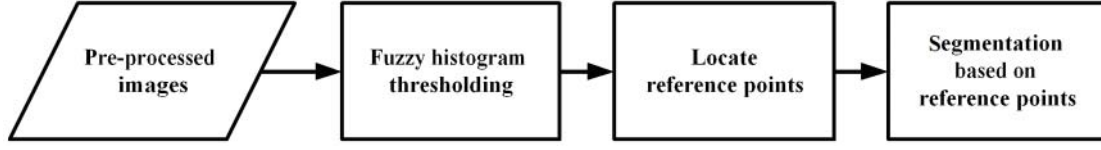


Fig. 3. Flowchart of the image segmentation stage.

2.2. Image Segmentation

The flowchart of the image segmentation procedure for our approach is shown Fig 3. It is made up of the following: the detailed algorithms for fuzzy histogram thresholding, the locating of the reference points, and the segmentation based on reference points. The reference points were determined based on human anatomy as well as physicians' recommendations.

2.2.1. Histogram thresholding using fuzzy sets

In order to locate typical reference points in the skeleton, the pixels of soft tissue were compressed and the pixels of bone around typical reference points were reserved. By using fuzzy sets for histogram thresholding, Tobias and Seara (2002) demonstrated successfully in separation background from object in multimodal and bimodal histogram images. In this study, we employed this algorithm to classify soft tissue and bone regions; the thresholding algorithm can be summarized as follows.

Set \mathbf{U} be the universe of discourse (all pixels in an image), with a generic element denoted by x_i : $\mathbf{U} = \{x_1, x_2, \dots, x_{\max}\}$. A fuzzy set \mathbf{A} in \mathbf{U} is defined as:

$$\mathbf{A} = \{(x_i, \mu_{\mathbf{A}}(x_i))\}, \quad x_i \in \mathbf{U} \quad (3)$$

The fuzzy set \mathbf{A} is characterized by the function $\mu_{\mathbf{A}}(x_i)$. In this study, the S -function is used to model the membership function. The S -function is defined as:

$$\mu_{A_s}(x) = S(x; a, b, c) = \begin{cases} 0, & x \leq a \\ 2\{(x-a)/(c-a)\}^2, & a < x \leq b \\ 1 - 2\{(x-c)/(c-a)\}^2, & b < x \leq c \\ 1, & x > c. \end{cases} \quad (4)$$

The parameter b is given by $b = (a + c) / 2$, with $\mu_{A_s}(b) = 0.5$. The bandwidth of the function is defined as $\Delta b = b - a = c - b$. The Z-function is derived from the S-function as below:

$$\mu_{A_z}(x) = Z(x; a, b, c) = 1 - S(x; a, b, c). \quad (5)$$

The nearest ordinary set of \mathbf{A} is denoted as $\underline{\mathbf{A}}$, its membership function is given by

$$\mu_{\underline{\mathbf{A}}}(x_i) = \begin{cases} 0, & \text{if } \mu_{\mathbf{A}}(x_i) < 0.5 \\ 1, & \text{if } \mu_{\mathbf{A}}(x_i) \geq 0.5. \end{cases} \quad (6)$$

In Kaufman's definition, the index of fuzziness (IF) (1975) is obtained by measuring the distance between \mathbf{A} and $\underline{\mathbf{A}}$. Such an index is defined as:

$$\psi_k(\mathbf{A}) = \frac{2}{n^{1/k}} d_k(\mathbf{A}, \underline{\mathbf{A}}) \quad (7)$$

where $d_k(\mathbf{A}, \underline{\mathbf{A}})$ is a measurement of distance and n is the number of elements in \mathbf{A} . The $d_k(\mathbf{A}, \underline{\mathbf{A}})$ is calculated by

$$d_k(\mathbf{A}, \underline{\mathbf{A}}) = \left(\sum_{i=1}^n (\mu_{\mathbf{A}}(x_i) - \mu_{\underline{\mathbf{A}}}(x_i))^k \right)^{1/k}. \quad (8)$$

We set $k = 1$, then the IF can be simplified as follows:

$$\begin{aligned} \psi_k(\mathbf{A}) &= \frac{2}{n} \sum_{i=1}^n |\mu_{\mathbf{A}}(x_i) - \mu_{\underline{\mathbf{A}}}(x_i)| \\ &= \frac{2}{n} \sum_{i=1}^n \min(\mu_{\mathbf{A}}(x_i), 1 - \mu_{\mathbf{A}}(x_i)) \\ &= \frac{2}{n} \sum_{k=p}^q (\min(\mu_{\mathbf{A}}(k), 1 - \mu_{\mathbf{A}}(k))) \cdot h(k) \end{aligned} \quad (9)$$

where $h(k)$ denotes the image histogram and p and q are the limits of the subset being considered. This algorithm applies the concept of *similarity*, a fuzzy set with a low index of fuzziness thus indicates that its elements are very similar to each other.

Two linguistic variables {soft tissue, bone} model was defined by two fuzzy subsets, denoted by **S** and **B** respectively. The fuzzy subsets **S** and **B** were associated with the histogram intervals $[x_{\min}, x_j]$ and $[x_r, x_{\max}]$ respectively, where x_j and x_r were the final and initial gray-level limits for these subsets, and x_{\min} and x_{\max} were the lowest and highest gray-levels of the image respectively. At the first IF measurement, we set $x_j = x_{\min} + 10$, and $x_r = x_{\max} - 10$. In this study, we modified the value of x_{\max} to the gray level where pixels accumulation from x_{\min} to the 97% of total pixels. The gray levels in each of these subsets have the intuitive property of belonging with certainty to the final subsets of the object (**O**) or background (**F**). That is, $\mathbf{S} \subset \mathbf{F}$ and $\mathbf{B} \subset \mathbf{O}$. Those subsets were located at the beginning and the end regions of the histogram. A *fuzzy region* placed between **S** and **B** was defined as depicted in Fig. 4. For classification procedure, a gray level picked from the *fuzzy region* was added to each of the seed subsets. By measuring the IF's of the subsets $\mathbf{S} \cup \{x_i\}$ and $\mathbf{B} \cup \{x_i\}$, x_i was assigned to the subset with the lower IF. By applying this procedure for all gray levels within the *fuzzy region*, each pixel was classified into soft tissue or bone. The proposed classification method is a comparison of IF measures and we needed to normalize those measures. This is achieved by first computing the IF's of the seed subsets **S** and **B**, and by computing a normalization factor α according to the following relationship.

$$\alpha = \frac{\psi_k(\mathbf{S})}{\psi_k(\mathbf{B})} \quad (10)$$

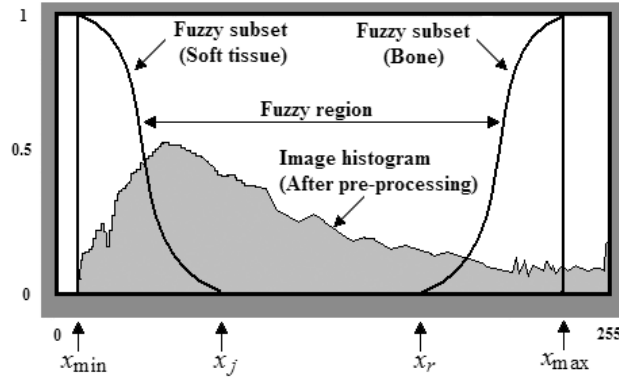


Fig. 4. The histogram and the characteristic functions for the seed subsets of a whole body bone image.

Where $\psi_k(\mathbf{S})$ and $\psi_k(\mathbf{B})$ are the IF's of the subsets \mathbf{S} and \mathbf{B} , respectively. Fig. 5 shows how the normalization works. The result of the histogram thresholding processing in anterior view is illustrated in Fig 2c, and is denoted as \mathbf{I}_{AP}^{fuzzy} . The result of the same process in the posterior view is denoted as \mathbf{I}_{PA}^{fuzzy} . After the histogram thresholding processing, the soft tissue regions were compressed and the thick/wide bones (e.g., shoulder, pelvic, and vertebral bones) were reserved for locating the reference points during the next step.

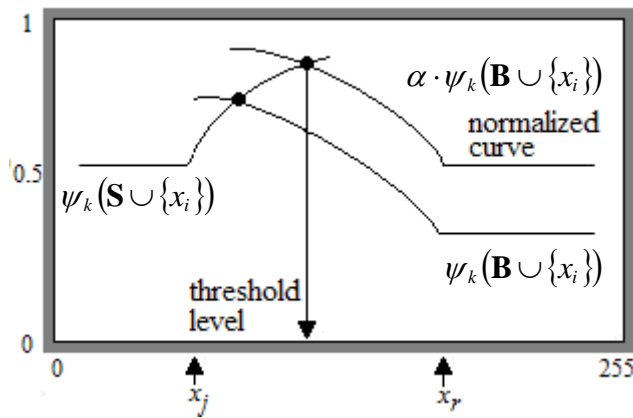


Fig. 5. Normalization step of the indices of fuzziness and deciding the threshold value.

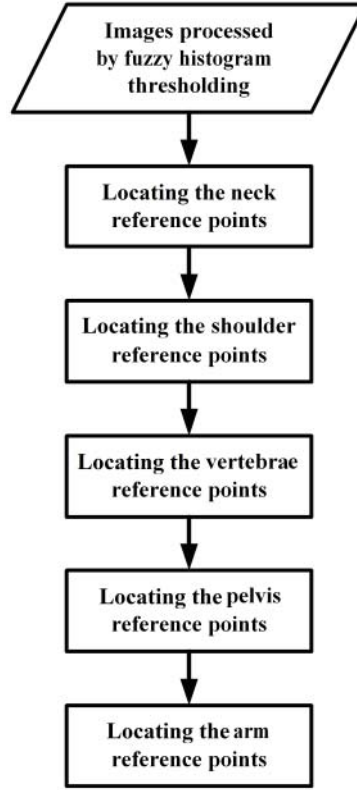


Fig. 6. Flowchart of locating the reference points.

2.2.2. Locating the reference points

The reference points of the neck, shoulder, vertebra, pelvis, and arms were determined sequentially as shown in the flowchart Fig. 6. The detailed algorithms are presented in the following subsections.

2.2.2.1. Locating the neck reference points

After performing the fuzzy histogram thresholding, image \mathbf{I}_{PA}^{fuzzy} was adopted to locate the neck reference points. By scanning each horizontal line from image top to the 25% image height in vertical direction, the horizontal widths formed by the most left non-zero pixel and the most right non-zero pixel in every row were calculated. The coordinates of the both ends of the minimum width were denoted as \mathbf{p}_{PA}^{neckl} and \mathbf{p}_{PA}^{neckr} ; these formed the neck reference points, which are labeled as ‘a’ and ‘b’ in Fig. 7a, respectively.

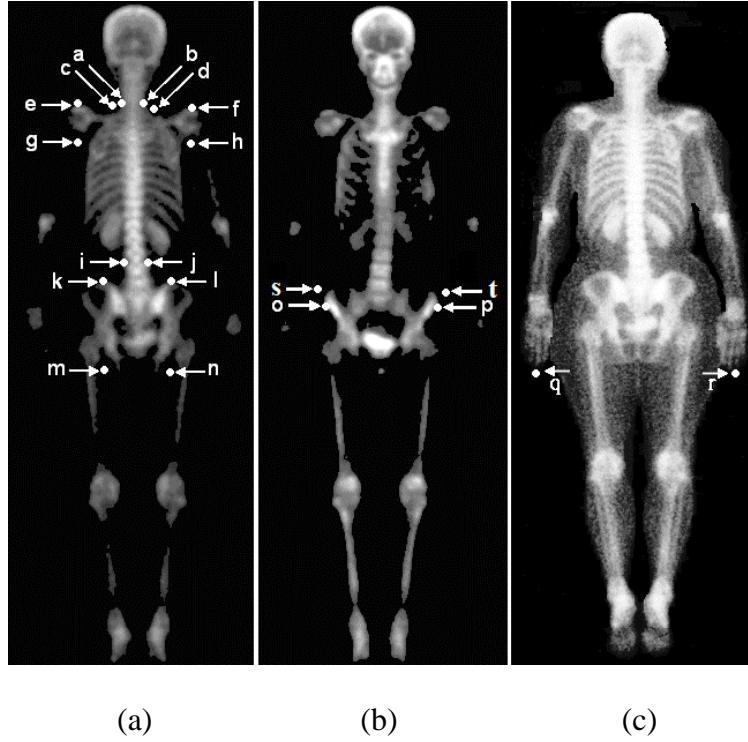


Fig. 7. Reference points demonstrated in image (a) \mathbf{I}_{PA}^{fuzzy} , (b) \mathbf{I}_{AP}^{fuzzy} , and (c) \mathbf{I}_{PA}^{pre} . The denoted symbols are mentioned in the text.

2.2.2.2. Locating the shoulder reference points

Image \mathbf{I}_{PA}^{fuzzy} was employed to find the shoulder apexes. From reference \mathbf{p}_{PA}^{neckl} to the 25% image height in vertical direction, the horizontal distances from left image border to the first non-zero pixel were calculated in each row. Once the distance difference ($=|\text{current distance} - \text{previous distance}|$) was greater 3 times than previous one, then the left apex of shoulder was located, which was denoted as \mathbf{p}_{PA}^{shol} (labeled ‘e’ in Fig. 7a). In a similar way, this approach was applied to locate the right apex of shoulder, which was denoted as \mathbf{p}_{PA}^{shor} (labeled ‘f’ in Fig. 7d).

In the horizontal direction, beginning from reference point \mathbf{p}_{PA}^{shol} to reference point \mathbf{p}_{PA}^{neckl} , finding the pixel (same horizontal coordinates with \mathbf{p}_{PA}^{shol}) that had the least gray-level value, and denoted it as \mathbf{p}_{PA}^{shoLS1} (labeled ‘c’ in Fig. 7a). In a similar way, the pixel with the least

gray-level value between \mathbf{p}_{PA}^{shor} and \mathbf{p}_{PA}^{neckr} was found, and denoted it as \mathbf{p}_{PA}^{shoRS1} (labeled ‘d’ in Fig. 7a). Beginning from \mathbf{p}_{PA}^{shoLS1} , the screening went along the lower left direction pixel by pixel, till the pixel which had the same horizontal coordinates as \mathbf{p}_{PA}^{shol} was found and denoted as \mathbf{p}_{PA}^{shoLS2} (labeled ‘g’ in Fig. 7a). Starting from \mathbf{p}_{PA}^{shoRS1} , the screening went along the lower right direction pixel by pixel, till the pixel which had the same horizontal coordinates as reference point \mathbf{p}_{PA}^{shor} was found and denoted as \mathbf{p}_{PA}^{shoRS2} (labeled ‘h’ in Fig. 7a). These four reference points were used to construct the boundary between shoulder and thorax.

2.2.2.3. Locating the vertebrae reference points

Due to the different distances from the collimators, the vertebrae are shown with better visibility in posterior view than in anterior view. Therefore, we adopted image \mathbf{I}_{PA}^{fuzzy} to locate the reference points for the vertebrae. By scanning each horizontal line from the 30% to 50% of the image height in vertical direction, the horizontal widths formed by the left most non-zero pixel and the right most non-zero pixel in every row were calculated, the coordinates of both ends of the minimum width were denoted as \mathbf{p}_{PA}^{verl} and \mathbf{p}_{PA}^{verr} for the vertebrae reference points, labeled as ‘i’ and ‘j’ in Fig. 7a respectively. These two reference points were directly mapped back to image \mathbf{I}_{AP}^{fuzzy} and denoted as \mathbf{p}_{AP}^{verr} and \mathbf{p}_{AP}^{verl} respectively.

2.2.2.4. Locating the pelvis reference points

The iliac activity is more prominent in anterior view and the sacral activity is higher in posterior view. Therefore, we used image \mathbf{I}_{AP}^{fuzzy} to locate the left and right extremities of pelvis, and image \mathbf{I}_{PA}^{fuzzy} to locate the apex and bottom reference points of pelvis.

Downward from the reference point \mathbf{p}_{PA}^{verl} in vertical direction, the horizontal distances between reference point \mathbf{p}_{PA}^{shol} and the left-first non-zero gray level pixel were calculated for each row. If the distance difference ($=|\text{current distance} - \text{previous distance}|$) exceeded 3 times than previous one, then the left-top of pelvis was located. In a similar way, this was applied to locate the right-top of pelvis. We denoted the left-top reference point as \mathbf{p}_{PA}^{pelLT} (labeled ‘k’ in Fig. 7a), and right-top reference point as \mathbf{p}_{PA}^{pelRT} (labeled ‘l’ in Fig. 7a). These two reference points were directly mapped back to image \mathbf{I}_{AP}^{fuzzy} and denoted as \mathbf{p}_{AP}^{pelRT} and \mathbf{p}_{AP}^{pelLT} respectively.

In image \mathbf{I}_{AP}^{fuzzy} , beginning from reference point \mathbf{p}_{AP}^{pelLT} at 50% image height in vertical direction, by horizontal distances were calculated between the reference point \mathbf{p}_{AP}^{shol} and the right-first non-zero pixel in each row. The right-end of the minimum distance row was the position of pelvis left-extremity and denoted as \mathbf{p}_{AP}^{pelLE} (labeled ‘o’ in Fig. 7b). In a similar way, this was possible to locate the right-extremity of pelvis and denoted as \mathbf{p}_{AP}^{pelRE} (labeled ‘p’ in Fig. 7b). These two reference points were mapped back to image \mathbf{I}_{PA}^{fuzzy} and denoted as \mathbf{p}_{PA}^{pelRE} and \mathbf{p}_{PA}^{pelLE} respectively.

In image \mathbf{I}_{PA}^{fuzzy} , starting from the reference point \mathbf{p}_{PA}^{pelLE} at 60% image height in vertical direction, we accumulated the horizontal counts of non-zero gray level pixels between the reference point \mathbf{p}_{PA}^{pelLT} and reference point \mathbf{p}_{PA}^{verl} in each row. If the accumulation value is zero, then the left-bottom reference point (same horizontal coordinates as reference point \mathbf{p}_{PA}^{pelLT}) was located and denoted as \mathbf{p}_{PA}^{pelLB} (labeled ‘m’ in Fig. 7a). Using a similar processing, it was possible to locate the right-bottom of pelvis, which was denoted as \mathbf{p}_{PA}^{pelRB} (labeled ‘n’ in Fig.

7a). In addition, two reference points (labeled ‘s’ and ‘t’ in Fig. 7b) were denoted as \mathbf{p}_{PA}^{segl} and \mathbf{p}_{PA}^{segr} and their coordinates were defined as:

$$\begin{aligned}\mathbf{p}_{PA}^{segl}(x, y) &= \mathbf{p}_{PA}^{pel_{LE}}(x - 10, y - 20) \\ \mathbf{p}_{PA}^{segr}(x, y) &= \mathbf{p}_{PA}^{pel_{LE}}(x + 10, y - 20)\end{aligned}\quad (11)$$

These two reference points were used to prevent from the miss-segmentation between the arms and pelvis.

2.2.2.5. Locating arm reference points

Low activity regions such as arms and legs were compressed in the global fuzzy subsets thresholding procedure. Therefore, we used image \mathbf{I}_{PA}^{pre} to locate the bottom reference points of arms. Downward from reference point $\mathbf{p}_{PA}^{pel_{LT}}$ to 60% image height in vertical direction, we accumulated the horizontal counts of non-zero gray level pixels between left image border and $\mathbf{p}_{PA}^{pel_{LE}}$ in each row. If the accumulation value was zero, then left-bottom arm reference point was located and denoted as $\mathbf{p}_{PA}^{arm_{LB}}$ (labeled ‘q’ in Fig. 7c). A similar processing was applied to locate the right-bottom of arm and this was denoted as $\mathbf{p}_{PA}^{arm_{RB}}$ (labeled ‘r’ in Fig. 7c).

2.2.3. Segmentation based on the reference points

The segmentation procedures demonstrated below were performed using the posterior view image and then directly mapped back to the anterior view image. The flowchart of final segmentation of the head, arms and shoulders, pelvis, legs, vertebra, and thorax portion are shown in Fig. 8.

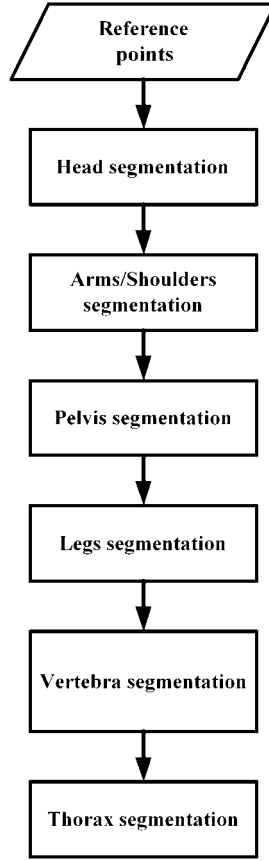


Fig. 8. Flowchart of the segmentation algorithm.

2.2.3.1. Head segmentation

In image \mathbf{I}_{PA}^{fuzzy} , the head region was segmented using the reference points \mathbf{p}_{PA}^{neckl} and \mathbf{p}_{PA}^{neckr} , and the left/right head extremities. The result of head segmentation is shown in Fig 9.

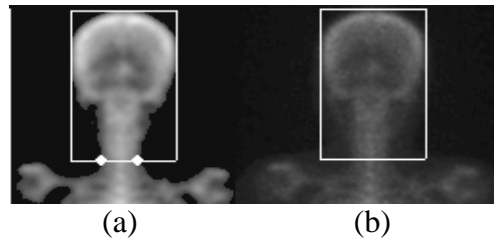


Fig. 9. The result of head segmentation in (a) image \mathbf{I}_{PA}^{fuzzy} , and mapped back to (b) image \mathbf{I}_{PA}^{org} .

2.2.3.2. Arms and shoulders segmentation

In image \mathbf{I}_{PA}^{fuzzy} , the left arm and shoulder regions were confined by the reference points \mathbf{p}_{PA}^{shol} , \mathbf{p}_{PA}^{shoLS1} , \mathbf{p}_{PA}^{shoLS2} , \mathbf{p}_{PA}^{segl} , and \mathbf{p}_{PA}^{armLB} , and the left shoulder region was confined by the reference points \mathbf{p}_{PA}^{shol} , \mathbf{p}_{PA}^{shoLS1} , and \mathbf{p}_{PA}^{shoLS2} (Fig. 10a).

In arm region, by scanning each horizontal line from the 30% to 70% height in vertical direction, the horizontal arm widths formed by the most left non-zero pixel and the most right non-zero pixel in each row were calculated, As a result, the maximum arm width can be obtained and its position was always at the elbow. Upward from the maximum arm width, if the arm width was less than the 30% of maximum arm width then the end of top-elbow had been reached. Downward from the maximum arm width, if the arm width was less than 30% of maximum arm width then the bottom-end of the elbow had been reached. The humerus region was then obtained between top-end of elbow and bottom of shoulder. Following this, the radius/ulna and palm regions were segmented in the same way. The whole process was then repeated to segment the right arm and shoulder regions.

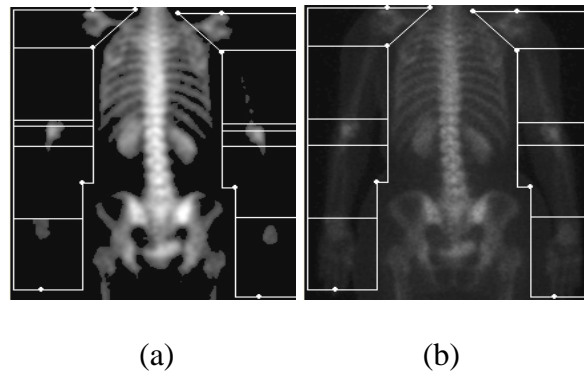


Fig. 10. The result of segmentation of the arm and shoulder regions into five different parts, namely the shoulder, humerus, elbow, radius/ulna and palm, in (a) image \mathbf{I}_{PA}^{fuzzy} , and mapped back to (b) image \mathbf{I}_{PA}^{org} .

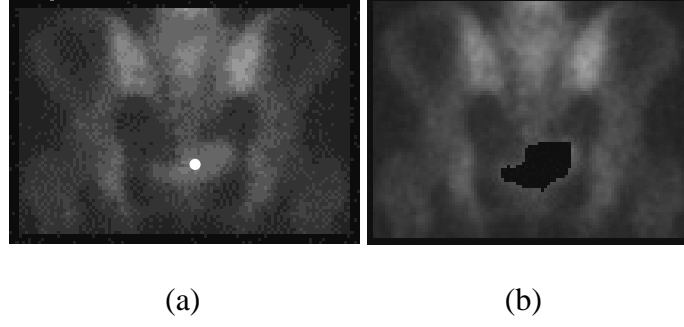


Fig. 11. Results of (a) pelvis segmentation and (b) urine activity removal.

2.2.3.3. Pelvis segmentation

As shown in Fig. 11, the pelvis image frame was confined by the reference points $\mathbf{p}_{PA}^{pel_{LT}}$, $\mathbf{p}_{PA}^{pel_{RT}}$, $\mathbf{p}_{PA}^{pel_{LB}}$, $\mathbf{p}_{PA}^{pel_{RB}}$, $\mathbf{p}_{PA}^{pel_{LE}}$, and $\mathbf{p}_{PA}^{pel_{RE}}$. In clinical practice, residual urine activity in bladder was commonly seen. To reduce the chance of miss-interpreting the bladder activity as a lesion, the urine activity must be removed.

We defined the height and width of pelvis region as h and w respectively, and a sub-region on pelvis was denoted as **SP**. the upper side from pelvis region to **SP** was $0.6h$, the lower side from **SP** to pelvis region was $0.2h$, the left side from pelvis to **SP** was $0.3w$, and the right side from **SP** to pelvis region was $0.3w$. Based on anatomy knowledge, **SP** is the most possible bladder region. Bladder activity can be removed by finding the maximum gray-level (labeled with white spot in Fig. 11a) pixel in **SP**. Region-growing can then start from this pixel, the end of the growing was set to 60% of the maximum gray-level. The result of removing the residual urine activity is shown in Fig. 11b.

2.2.3.4. Legs segmentation

Image \mathbf{I}_{PA}^{fuzzy} was applied to segment legs, and the reference points $\mathbf{p}_{PA}^{pel_{LB}}$, $\mathbf{p}_{PA}^{pel_{RB}}$, \mathbf{p}_{PA}^{segl} , and \mathbf{p}_{PA}^{segr} confined the leg area. Using the center line of legs, the leg area was separated into left leg and right leg (Fig. 12a). In the left leg region, by scanning each horizontal line from the

30% to 70% of the height of the left leg region in vertical direction, the widths formed by the most left non-zero pixel and the most right non-zero pixel in every row were calculated, the maximum width was always at knee. Upward from the maximum leg width, if the leg width was less than 30% of the maximum leg width then the position of top-end of knee was obtained. Downward from the maximum leg width, if the leg width was less than 30% of the maximum leg width, then the position of bottom-end of knee was located. Through the above processing, the femur region can be obtained by positions between the top-end of knee and the top-end of leg region. The knee area was obtained between the positions of top-end knee and the bottom-end knee. By adopting a similar approach to that described above, the tibia/fibula and foot areas can be segmented from the left leg area. Thereafter, the method of segmentation for the left leg region can be performed on the right leg region. The results can be shown in Fig. 12.

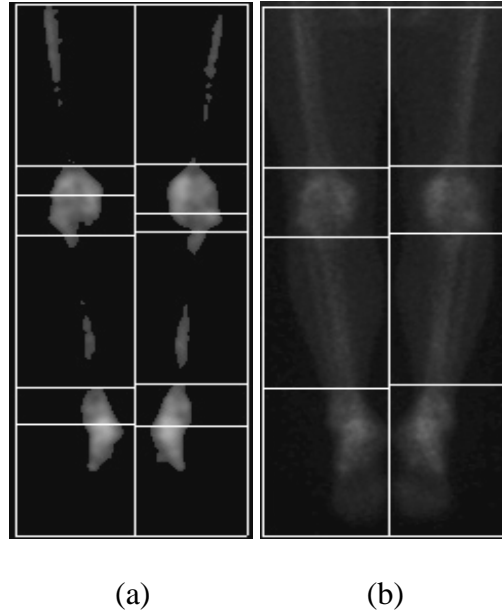


Fig. 12. The segmentation result for the leg region (four different parts: femur, knee, tibia/fibula, and foot) in (a) image I_{PA}^{fuzzy} , then mapped back to (b) image I_{PA}^{org} .

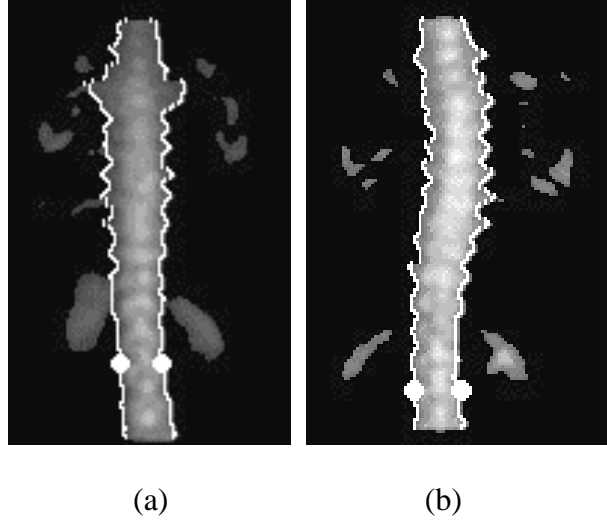


Fig. 13. Vertebra segmentations of (a) a patient with a normal straight spine and (b) another patient with a scoliosis spine.

2.2.3.5. *Vertebrae segmentation*

After the earlier segmentations, the trunk including the thoracic and abdominal parts, is left for further vertebrae segmentation. A histogram thresholding using fuzzy sets as mentioned in section 2.2.1. is applied to the local trunk area on image \mathbf{I}_{PA}^{pre} . There is no bone or high activity kidney surrounding the partial vertebrae between the vertebrae reference points and pelvis. Therefore, this partial vertebrae region in this area was obtained by simply segmentation using the above thresholding approach. However, this method of vertebrae segmentation meets challenges in the region between the vertebrae reference points and the neck reference points due to accumulation of radioactivity over kidneys and/or ribs in most of our cases. A more detailed segmentation procedure was performed in this area and is summarized below:

The left vertebrae edge detection between reference point \mathbf{p}_{PA}^{verl} and \mathbf{p}_{PA}^{neckl} was started from the reference point \mathbf{p}_{PA}^{verl} , and then determined the subsequent upward edge points by moving the reference point \mathbf{p}_{PA}^{verl} vertically to next pixel. If the next pixel is zero in gray-level scale, the coordinates value of left vertebra edge can be assigned to the first right non-zero gray-

level pixel at the same horizontal plan. However, if the next pixel is non-zero in gray-level scale, the first left zero pixel is presumed to be a possible edge point. The possible edge point will be checked by measuring the horizontal distance between the possible edge point and the beginning point. If the distance is less than 4 pixels, the possible edge point will be marked as the left vertebra edge. On the other hand, if the distance is over 4 pixels, the left vertebra edge is assigned to be the beginning point of this horizontal plane. Then assign the vertebra edge obtained by the above method as the new starting point and continue the procedures as above, till all left vertebra edges were marked. The right vertebrae edge points are marked with in a similar way (Fig. 13a).

As shown in Fig. 13b, this algorithm was also able to successfully segment the vertebral region of a scoliosis patient.

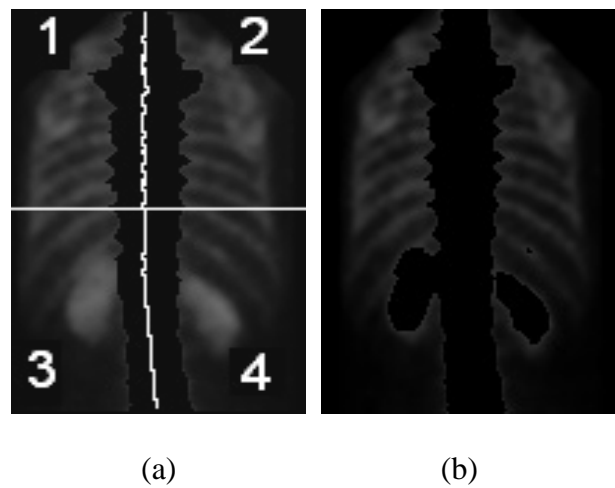


Fig. 14. Results of (a) thorax segmentation and (b) urine removal.

2.2.3.6. *Trunk (thorax and abdominal) segmentation*

Through the above processing, the vertebrae are segmented as separate from the rest of the trunk (thorax and abdominal) region (Fig. 14a). Then the rest of the trunk region was further divided into four areas. The mean gray-level values in area-1 and area-3 were calculated, if the mean gray-level value of area-3 was greater than area-1, there was highly possible that

urine remained in kidney region. If true, the urine activity in the kidney was removed as follows:

Firstly, the maximum gray-level value pixel in the area with a vertical range between 50% and 80% height of area-3, and horizontal range was between 50% and 90 % width of area-3 was found, then the maximum gray-level value pixel was used as the starting pixel of region-growing algorithm to remove the urine activity from the kidney. The end growing gray-level was set to the 60% of maximum gray-level value. The right urine activity in this kidney was removed by the same method. The result is shown in Fig. 14b.

The results for the segmentation phase of a whole body bone image are shown in Fig. 15. They are used during for the further process of lesion detection.

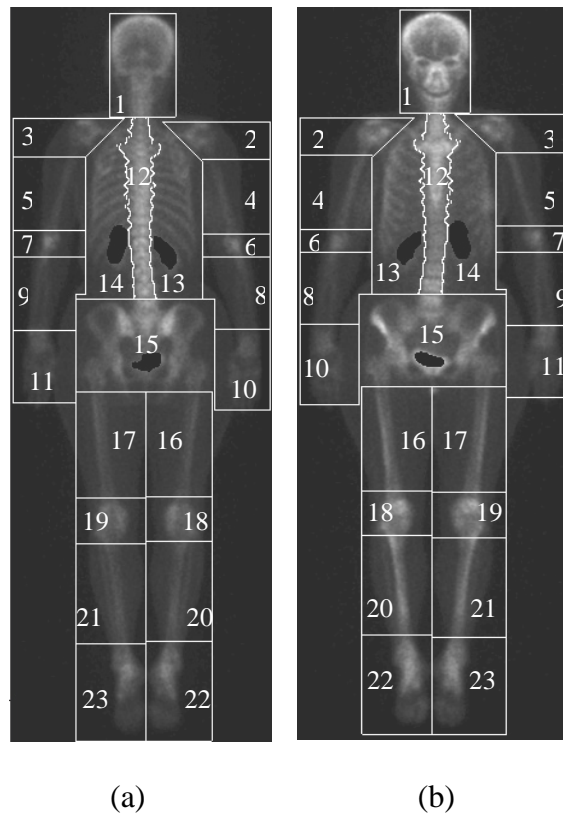


Fig. 15. Results of 23 segmented regions in (a) anterior view and (b) posterior view respectively.

By applying the segmentation algorithms as mentioned above, the regions of head, hand, vertebra, and thorax were successfully segmented apart from the whole body bone scan image without error. For the pelvis and leg regions, only in 3 images out of 162 patient images did miss-segmentation occur due to urine contamination below the pelvis.

2.3. Lesion Gray Level Determination

The differences in bone scan acquisition time, post injection waiting time, distance between patient and detectors, and the constitution of patients result in gray level distributions in the same portion of the skeleton among different patients being highly variable (Fig. 16). Therefore, it is impossible to simply use a single gray level threshold to differentiate between pathological lesions and normal bones.

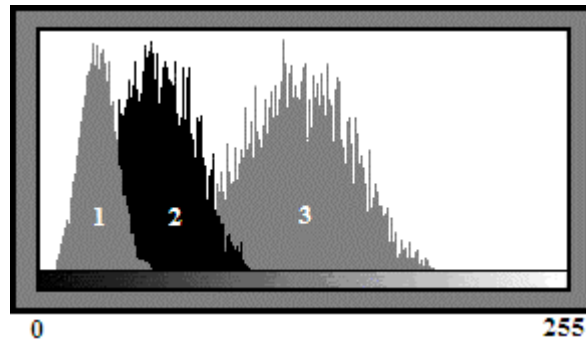


Fig. 16. A wide gray level distribution range in the spine portion of three normal patients.

The high turn-over rate of the bony components in each segmented bone region results in heterogeneous gray-scale distribution. A larger distribution range in gray level histogram results in larger standard derivation (*sd*) for each location. In other word, a large standard derivation value might indicate the existence of a possible bone lesion. Therefore, we introduced and defined the following parameters to evaluate the heterogeneity in each segmented bone region.

$$mean = \bar{x} = E(x) = \sum_{x=x_{\min}}^{x_{\max}} x \cdot p(x) \quad (12)$$

$$standard\ derivation = sd = \sqrt{\sum_{x=x_{\min}}^{x_{\max}} (x - \bar{x})^2 \cdot p(x)}. \quad (13)$$

For a test image, we are concerned about high activity lesion areas more than the low activity areas, a more appropriate parameter was defined as follow:

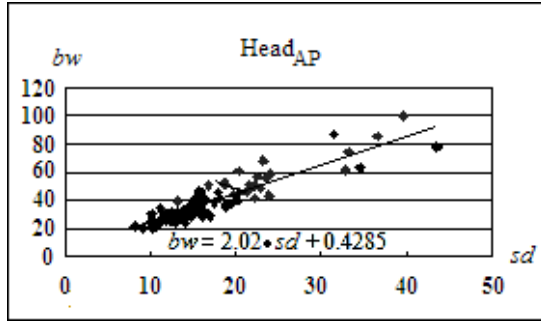
$$bandwidth_{test} = bw_{test} = max\ gray-level - mean\ gray-level. \quad (14)$$

A least squares estimation was adopted to determine the lesion gray levels. First of all, we recruited whole body bone scan raw data from 100 normal patients and computed the values for bandwidth (bw_{ref}) and standard derivation (sd) of each normal segmented bone region.

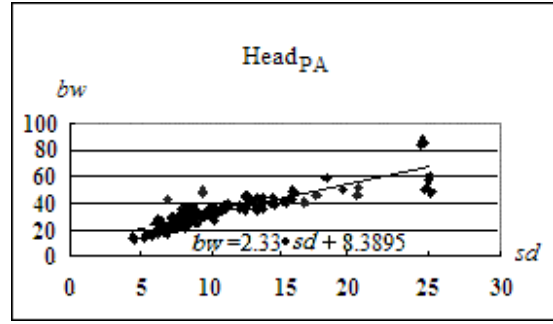
Then, a formula was obtained by the least squares estimation that is as follow:

$$bandwidth_{ref} = bw_{ref} = a \cdot sd + b + \varepsilon. \quad (15)$$

Where a and b are the constant parameters of the formula which were different for each segmented region and ε is assumed to be uncorrelated, with a mean of 0 and constant variance. Two examples of the regression lines are shown in Fig. 17. All regression formulas are shown in Table 1. When we wanted to determine the status of each bone location for a test image, we first calculated the mean gray-level and the sd in the specific region. Next, we obtain the normal bandwidth (bw_{ref}) by substituting this sd into the equation. Finally, if the bandwidth of a test image (bw_{test}) is greater than the normal bandwidth (bw_{ref}), this pixel is highly suspicious and may be a pathological lesion.



(a)



(b)

Fig. 17. Two examples of the regression analysis for the head in (a) anterior view and (b) posterior view.

Table 1. The regression formulas obtained by regression analysis for each segmented region.

| Region | Regression Formula ($bw = a \cdot sd + b$) | Region | Regression Formula ($bw = a \cdot sd + b$) |
|------------------------|---|-------------------------|---|
| Head (AP) | $bw = 2.02 \cdot sd + 0.4285$ | Palm (AP/PA) | $bw = 2.58 \cdot sd + 3.0534$ |
| Head (PA) | $bw = 2.33 \cdot sd + 8.3895$ | Thorax (AP) | $bw = 4.01 \cdot sd + 8.0989$ |
| Vertebra (AP) | $bw = 2.01 \cdot sd + 3.5561$ | Thorax (PA) | $bw = 3.13 \cdot sd + 6.9867$ |
| Vertebra (PA) | $bw = 2.35 \cdot sd + 3.8143$ | Pelvis (AP) | $bw = 3.29 \cdot sd + 8.8997$ |
| Shoulder (AP) | $bw = 2.53 \cdot sd + 1.1546$ | Pelvis (PA) | $bw = 3.41 \cdot sd + 3.5013$ |
| Shoulder (PA) | $bw = 2.55 \cdot sd + 2.5345$ | Femur (AP/PA) | $bw = 2.83 \cdot sd + 6.0323$ |
| Humerus (AP/PA) | $bw = 3.05 \cdot sd + 4.5935$ | Knee (AP/PA) | $bw = 2.07 \cdot sd + 6.5583$ |
| Elbow (AP/PA) | $bw = 2.29 \cdot sd + 2.0993$ | Tibia/Fibula (AP/PA) | $bw = 3.09 \cdot sd + 5.1613$ |
| Radius/Ulna (AP/PA) | $bw = 3.15 \cdot sd + 1.3939$ | Foot (AP/PA) | $bw = 2.95 \cdot sd + 0.9126$ |

3. EXPERIMENTAL RESULTS

3.1. Software Programming and Data Acquisition

In order to evaluate the proposed algorithm in this study, we implemented a program constructed using C⁺⁺ Builder 6.0, and performed experiments on an image database from the Department of Nuclear Medicine, Buddhist Tzu Chi General Hospital, Hualien, Taiwan. At 3 hours after intravenous injection of 750 MBq ^{99m}Tc-MPD, the whole body bone scan images were acquired by a dual-head gamma camera model GE Infinia with two heads equipped with low energy high-resolution (LEHR) collimators. The scan speed was 10 cm/min with no pixel zooming. Energy discrimination was provided by a 20% window centered on the 140 keV of ^{99m}Tc-MPD. The whole body field was used to record anterior and posterior views digitally with a resolution of 1024 pixels × 256 pixels. Images represented the counts of detected gamma rays at each pixel with 16-bit grayscale depth.

To obtain lesion thresholds in the various segmented regions, the ranges and standard deviations of gray-level distributions were obtained from 100 normal whole body bone patient images. The 62 random selected patient whole body scan images were used for testing. These 62 test cases were recruited from lung cancer and breast cancer patients who had undergone a whole body bone metastatic survey between January and April 2004. They were selected from a pool of 245 patients. In these 62 cases, there were only 6 “disease free” scans. Majority of elderly patients had joint arthritis and degenerative spine disease. Only 13 patients have metastatic bone disease. The 100 normal individuals were not included in the testing set. The detection rate of true abnormalities and the number of false lesion detections per scan image as performance indices were used to evaluate the proposed system.

3.2. Results

Table 2 shows the result of the evaluation. There were 241 true abnormalities present within the 62 abnormal images. In total, 222 abnormalities were detected. The detection rate was 92.1% (222 of 241), and there were 7.58 false detections per patient scan image.

Table 2. Detection rates and mean number of false detections across 62 test images divided into six parts.

| Region | Abnormalities | Detected | False detections |
|---------------------------|---------------|----------------------|------------------|
| Head | 31 | 31 (100%) | 67 |
| Spine | 81 | 72 (89%) | 64 |
| Chest | 38 | 34 (90%) | 71 |
| Pelvic | 32 | 27 (84%) | 71 |
| Hand | 23 | 23 (100%) | 112 |
| Leg | 36 | 35 (97%) | 85 |
| Total | 241 | 222 (92.1%) | 470 |
| Average (= Total / 62) | 3.89 | 3.58 | 7.58 |

The final results of this test for one case are shown in Figs. 18 and 19, where the arrow-pointed regions represent the detected lesions by our proposed set of algorithms. The positions labeled with circles are the false positive lesions detected by our system.

4. CONCLUSION

In this study, a fully automatic CAD system for nuclear medicine, a whole body bone scan algorithm was developed. By applying the proposed procedure, we obtain a pathologic lesion detection rate of 92.1% with an acceptable 7.58 false detections per patient scan image. The results of this work achieved the initial goals of progress towards a fully automatic processing system with high sensitivity and an acceptable false positive rate that could be used for clinical diagnosis. Based on this proposed approach, these satisfactory results encourage us to further develop a new and more efficient approach that can also be applied to tomographic images.

ACKNOWLEDGMENTS

This work was supported in part by the National Science Council, Taiwan, Republic of China, under the grant number NSC89-2218-E-155-001.

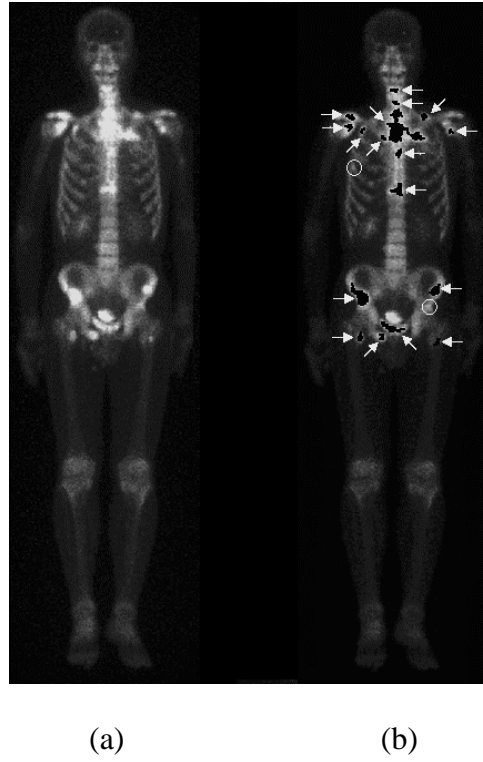


Fig. 18 The anterior view of (a) an original whole body image, and (b) the diagnosis result. The 17 arrow-pointed locations are true abnormal locations of the patient, and the 2 circle-marked locations are false positive locations.

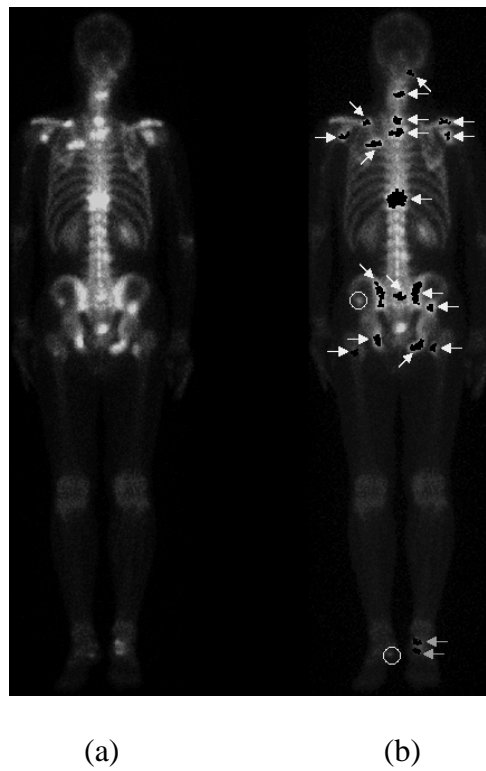


Fig. 19 The posterior view of (a) an original whole body image, and (b) the diagnosis result. The 19 arrow-pointed locations are true abnormal locations of the patient, and the 2 circle-marked locations are false positives locations.

REFERENCES

- Brown, M. L., 1989. The role of radionuclide in the patient with osteogenic sarcoma, *Seminars in Roentgenology* 24, 185-192.
- Erdi, Y. E., Humm, J. L., Imbriaco, M., Yeung, H., Larson, S. M., 1997. Quantitative bone metastases analysis based on image segmentation, *Journal of Nuclear Medicine* 38(99), 1401-1406.
- Kaufmann, A., 1975. *Introduction to the Theory of Fuzzy Subsets*. Academic Press, New York.
- Šajn, L., Kukar, M., Kononenko, I., Milčinski, M., 2005. Computerized segmentation of whole-body bone scintigrams and its use in automated diagnostics, *Computer Methods and Programs in Biomedicine* 80, 47-55.
- Sadik, M., et al, 2006. A new computer-based decision-support system for the interpretation of bone scans. *Nuclear Medicine Communication* 27(5), 417-423.
- Robey, E. L., Schellhanner, P. F., 1984. Solitary lesions on bone scan in genitourinary malignancy, *Journal of Urology* 132(5), 1000-1002.
- Tobias, O. J., Seara, R., 2002. Image segmentation by histogram thresholding using fuzzy sets, *IEEE Transactions on Image Processing* 11, 1457-1465.
- Yin, T. K., Chiu, N. T., 2004. A computer-aided diagnosis for locating abnormalities in bone scintigraphy by a fuzzy system with a three-step minimization approach, *IEEE Transactions on Medical Imaging* 23, 639-654.